Received: 14 September 2019 | Revised: 15 January 2020 | Accepted: 3 February 2020 | Published on: 4 May 2020

DOI: 10.1002/qj.3786

Quarterly Journal of the Royal Meteorological Society

RESEARCH ARTICLE

Forcing of the Martian polar annulus by Hadley cell transport and latent heating

R. K. Scott[1] | W. J. M. Seviour[2] | D. W. Waugh[3]

[1]School of Mathematics and Statistics, University of St Andrews, St Andrews, UK

[2]Cabot Institute, School of Geographical Sciences, University of Bristol, Bristol, UK

[3]Department of Earth and Planetary Sciences, Johns Hopkins University, Baltimore, Maryland

Correspondence
R. K. Scott, School of Mathematics and Statistics, University of St Andrews, North Haugh, St Andrews, KY16 9SS, UK.
Email: rks4@st-andrews.ac.uk

Abstract

A hierarchy of idealized models is used to investigate the roles of Hadley cell forcing and latent heat release from carbon dioxide condensation in determining the annular potential vorticity structure of the Martian winter polar vortex. The angular momentum conserving the Hadley cell model of Lindzen and Hou with summer hemisphere heating maximum of appropriate strength and latitude produces a strong westerly jet near 60°N, which is similar in strength to the winter polar night jet on Mars. Although the corresponding potential vorticity profile in the angular momentum conserving and thermal wind regions has no annular structure resembling the Martian one, there is an implied δ-function at the discontinuity in zonal wind. This δ-function is smoothed out by explicit diffusion in full axisymmetric model integrations forming a partial annular structure, though a local maximum in potential vorticity at the pole persists and is further enhanced when cooling representing the polar night is included. A distinct polar minimum and clear annular potential vorticity structure are obtained, however, when an additional representation of polar latent heating is also included. Full eddy-permitting shallow-water model integrations confirm the basic structure obtained by the axisymmetric model and suggest a nominal value of viscosity appropriate as a representation of the effects of eddy mixing. Instability of the polar annulus leads to vacillation-type behaviour involving eddy growth and annulus disruption, followed by re-formation under the influence of radiative relaxation. The degree of transience and mean eddy activity both show an increase with stronger latent heating and the resulting deeper polar potential vorticity minimum, showing that mixing in polar regions may be dependent on details of polar carbon dioxide condensation. Vacillation time-scales are also shown to vary with radiative time-scales, but through a modification of instability growth rate rather than as a result of direct radiative restoration.

KEYWORDS

Hadley cell, latent heating, Mars, polar vortex, potential vorticity

 © 2020 Royal Meteorological Society

1 | INTRODUCTION

The Martian polar atmosphere in winter is characterized by a strong cyclonic zonal mean circulation, the detailed structure of which has been inferred from the temperature retrievals of the *Mars Global Surveyor* (Banfield *et al.*, 2004; McConnochie, 2007), as well as model studies (Barnes and Haberle, 1996; Waugh *et al.*, 2016) and reanalysis products (Montabone *et al.*, 2006; Greybush *et al.*, 2012; Montabone *et al.*, 2014). The polar winds broadly resemble those of the Earth's winter stratospheric polar vortex but with some important differences, in particular regarding the potential vorticity distribution and the forcing mechanisms responsible for creating the circulation (see, e.g., Mitchell *et al.*, 2015 for a comparative overview). Specifically, the Martian polar vortex is observed to have an annular structure in potential vorticity, which has been proposed to be related to latent heat release from the condensation of carbon dioxide in the extreme cold temperatures of the polar night (Toigo *et al.*, 2017). Since such a structure is expected to be unstable to horizontal wave perturbations, the observations raise the question of how it is sustained on time-scales of the seasonal cycle.

In contrast to that of the Earth, the Martian atmosphere does not have a distinct stratosphere; accordingly the Martian polar vortex may be considered as an essentially tropospheric feature. It is driven in part by the outflow from a broad Hadley cell extending from the Southern (summer) Hemisphere as far as 60 or 70°N and the associated angular momentum transport within this cell (e.g., Leovy, 2001). As such, it may be more correctly likened to the Earth's subtropical jet (Waugh *et al.*, 2016). Because the Martian surface has no oceans and a relatively thin atmosphere, the effective solar heating of the atmosphere is more strongly controlled by the planetary obliquity than on Earth. Consequently, there is greater hemispheric asymmetry in the location of maximum heating during the seasonal cycle and greater asymmetry between winter and summer Hadley cell branches. Additionally, large zonal mean topography and, to a lesser extent, orbital eccentricity both contribute to higher effective summer heating in the Southern Hemisphere and consequently a stronger and broader Northern Hemisphere winter Hadley cell branch than its Southern Hemisphere winter counterpart (Richardson and Wilson, 2002; Zalucha *et al.*, 2010). For this reason, the Martian polar vortex is significantly stronger and more defined in the Northern Hemisphere winter.

Details of the structure of the Martian polar vortex are tied to the nature of the angular momentum within the Hadley cell. Angular momentum is transported up to the edge of the cell but not significantly beyond it, where the zonal flow is closer to a state of thermal wind balance with the radiative equilibrium temperature. Depending on the details of the radiative equilibrium over the pole, the potential vorticity resulting from the Hadley cell could in certain circumstances be maximized near the vortex edge, accounting for the observed annular structure, which has a minimum in potential vorticity over the pole and a maximum around 70°N (Mitchell *et al.*, 2015; Waugh *et al.*, 2016). However, the connection between the Hadley cell and the polar vortex structure has not been studied in detail. As will be seen further below, details of the potential vorticity distribution over the pole depend on the relative strengths of Hadley cell angular momentum transport and polar diabatic forcing. Diabatic forcing on Mars is not limited to cooling during the winter night, where temperatures are low enough that latent heat release from carbon dioxide condensation may play a significant role in the seasonal mean temperature budget. In particular, a recent modelling study found that when parametrization of carbon dioxide condensation was removed, the polar vortex remained monopolar and did not develop any annular structure (Toigo *et al.*, 2017).

It is well known from theory and numerous modelling studies that annular distributions of potential vorticity can in general be shear unstable (e.g. Waugh and Dritschel, 1991; Dritschel and Polvani, 1992). In the context of the Martian vortex, Seviour *et al.* (2017) demonstrated in a spherical shallow-water model that in the absence of any external forcing, an annular structure broadly representative of the observed potential vorticity rapidly collapses into a monopolar structure. Seviour *et al.* (2017) examined both the linear and nonlinear nature of this barotropic instability. Typical vortex geometries were found to be linearly unstable to zonal wavenumbers in the range 3–6, with maximum growth rates on time-scales in the range of 1–3 sols. Consequently, in nonlinear calculations the annular structure was found to persist when the vortex was sustained by a relaxational forcing to the initial annular structure on comparable time-scales, which is broadly representative of the radiative relaxational time-scale on Mars (Eckermann *et al.*, 2011). Seviour *et al.* (2017) found that when relaxation time-scales were much longer than the time-scale for instability the late-time vortex became more monopolar, whereas when relaxation time-scales were shorter the late-time vortex remained more strongly annular. When instability and relaxational time-scales are comparable, the nonlinear eddy motions that exist in the statistically stationary state represent a balance between zonal forcing and eddy growth due to instability. Observations indicate zonal asymmetries that may indeed represent coherent potential vorticity structures resulting from the instability of a continuously forced annulus.

In this article, we consider the extent to which the simple Hadley cell models of Held and Hou (1980) and Lindzen and Hou (1988), which have a long history of application in the atmospheric circulation of the Earth, may provide insight into how the balance of dynamical forcings controls the structure of the Martian polar vortex. Such axisymmetric models have also been applied to the study of Martian great dust storms (Schneider, 1983). In addition to examining the purely axisymmetric formation mechanisms, we also consider how the annular potential vorticity distribution persists in the presence of shear instability and how the saturation of nonlinear eddy motions arising from the instability depends on the relative strengths of Hadley cell transport and diabatic forcing. In the non-axisymmetric calculations, this article extends the work of Seviour *et al.* (2017) primarily in that the forcing is a now closer representation of the angular momentum transport on Mars. Specifically, the polar annulus is forced not through a direct relaxation to a prescribed annular structure, but rather through a relaxation to an unrealizable equilibrium state that implies the development of a latitudinally broad Hadley cell.

The article is structured as follows. In section 2, we review the angular momentum conserving (AMC) models of steady axisymmetric flow and consider the structure of the solutions in the parameter regime relevant for the Martian winter solstice. We also introduce simple representations of diabatic cooling and heating within the thermal equilibrium of the polar region. In section 3, we examine the extent to which the AMC model solutions are realized in an axisymmetric shallow-water model with relaxation to a similar thermal equilibrium profile, and examine how the inviscid solution is approached with decreasing viscosity. We also briefly consider how this model, for a given viscosity appropriate to nonlinear eddy mixing, may be used to quickly infer the zonal mean circulation under different conditions, varying the planetary obliquity and solar forcing. In section 4, we consider the competition between dynamical instability and forcing by examining a full eddy-resolving shallow-water model. The dependence of the eddy structure of the annulus on different forcing parameters is also considered. Section 5 concludes.

2 | THE LH88 AMC MODEL

Held and Hou (1980) and Lindzen and Hou (1988) (hereafter LH88) examined the steady-state axisymmetric circulation generated by solar heating that maximized in the Earth's tropics. The symmetric case in which the heating maximum is located exactly on the equator (Held and Hou, 1980) can be considered as representing the equinox conditions, while the off-equator case (LH88) pertains to solsticial or seasonally evolving conditions and is the relevant model for the present study. In these models, the heating is represented by a relaxation to a radiative-convective equilibrium temperature θ_e. The models are based on the result that the zonal flow in thermal wind balance with such heating would have a surface wind maximum that exceeds the planetary rotation, which is unrealizable in the absence of additional forcings (Hide, 1969). Thus the radiative equilibrium state cannot be attained in a latitudinal band surrounding the heating maximum, and the difference between the actual temperature θ and θ_e implies the existence of a transverse circulation in the meridional plane. The existence of the transverse circulation in turn means that the absolute angular momentum must be constant within such a region.

The model is made explicit by consideration of the zonal momentum equation, which for steady axisymmetric flow simplifies to

$$v\frac{dm}{d\mu} = 0, \tag{1}$$

where $m = a\cos\phi(a\Omega\cos\phi + u)$ is the absolute angular momentum, u and v are zonal and meridional components of velocity, ϕ is latitude, $\mu = \sin\phi$, Ω is the planetary rotation, and a is the planetary radius. Equation 1 can be satisfied by the vanishing of either factor. Thus, inside the angular momentum conserving (AMC) region near the heating maximum, $v \neq 0$ but the flow has constant angular momentum, $dm/d\mu = 0$, or equivalently zero absolute vorticity; the associated zonal flow is in thermal balance with some $\theta \neq \theta_e$. Outside the AMC region, $v = 0$ and the zonal wind is in thermal balance with θ_e.

LH88 used a hemispherically asymmetric equilibrium heating with a latitudinal profile of the form

$$\theta_e/\theta_0 = 1+\Delta\left(\frac{1}{3} - (\sin\phi - \sin\phi_0)^2\right), \tag{2}$$

where here θ_e represents an average in the vertical over the depth H of the troposphere. The heating has a maximum at latitude ϕ_0 and a horizontal temperature difference Δ. In their model formulation, the flow is assumed to be AMC between latitudes ϕ_s and ϕ_w, the summer and winter hemisphere termini, and in thermal wind balance poleward of these latitudes. The location of maximum ascent, ϕ_1, differs from the location of maximum heating, ϕ_0, such that the summer cell is significantly weaker than the winter cell. Indeed, one of the main conclusions of LH88 was that even weakly asymmetric forcing results in large asymmetry between the summer and winter cells, to the extent that the annual averaged transport of seasonally

varying heating must greatly exceed the transport due to the annually averaged heating.

For a specified asymmetry ϕ_0 and heating strength Δ, the latitudes ϕ_1, ϕ_s and ϕ_w are determined uniquely by matching conditions between the AMC and thermal wind regions, obtained from conservation of energy and continuity of temperature at ϕ_s and ϕ_w. The matching conditions were given in LH88's eqs. 8–11 and lead to a system of three nonlinear equations in the unknowns ϕ_1, ϕ_s and ϕ_w. For completeness and for ease of future use, we provide the equations in the Appendix. The main point, however, is that the solutions are controlled by just two parameters: the asymmetry ϕ_0 and the combination $R = B\Delta$, where $B = gH/a^2\Omega^2$ is a planetary Burger number. Thus the effects of the heating strength Δ and the physical planetary parameters affect the solution only in the combination $R = B\Delta$, rendering it unnecessary to consider these parameters in isolation. Here we use planetary parameters as given in Seviour *et al.* (2017), so that $L_D = \sqrt{gH}/2\Omega = 1800$ km with $a = 3390$ km, giving $B = 1.12$.

The AMC model is readily extended beyond the Earth regime to one that is more relevant to the Martian atmosphere simply by considering larger values of ϕ_0 and/or Δ, which can be increased until the northern edge of the AMC region coincides approximately with the observed extent of the Hadley cell on Mars. Figure 1 shows the latitudes ϕ_1, ϕ_s and ϕ_w as a function of ϕ_0 and for several values of $\Delta = RB$. The symbol $\phi_0 = 6°$ on the curve with the smallest Δ indicates the case considered in LH88's fig. 9c. For the Martian atmosphere, a winter terminus at approximately 60°N is appropriate and is indicated by a dashed horizontal line. The response at any point on this line can be obtained with an appropriate combination of ϕ_0 and Δ; three combinations are indicated that will be used for further analysis: $(\phi_0, \Delta) = (12°, 0.3)$, $(16°, 0.2)$ and $(20°, 0.15)$. As would be expected, the more symmetric the forcing (the smaller ϕ_0) the larger the Δ required to attain the same maximum latitude of the winter cell.

Profiles of θ/θ_0, vertically averaged zonal wind u and absolute vorticity ζ_a for three combinations of ϕ_0 and R with $\phi_w = 60°$ (indicated by the symbols in Figure 1) are shown in Figure 2. The change in the imposed temperature difference Δ can be seen in the profiles of θ and, to a lesser extent, in those of u and ζ_a. Essentially, the parameters controlling the summer and winter extents and the location of maximum extent all vary more or less similarly with ϕ_0; fixing ϕ_w thus results in similar, but not exactly the same, ϕ_s and ϕ_1 and a broadly similar parabolic form (in sine latitude) for u. The differences will be explored more in the eddy-resolving model below.

In all three cases, the absolute vorticity is exactly zero within the AMC region (bounded by the thin vertical lines) and equal to a profile in thermal wind balance

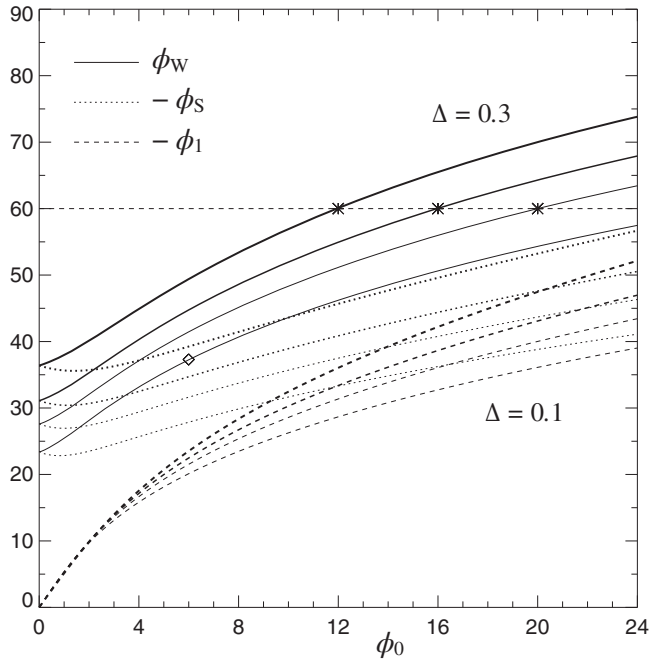

FIGURE 1 Transition latitudes for the angular momentum conserving (AMC) solutions of Lindzen and Hou (1988) (LH88). The values $\Delta = 0.1, 0.15, 0.2, 0.3$ are shown with increasing line thicknesses. Stars indicate the cases presented below; the diamond indicates that of LH88's fig. 9c

with θ_e outside. At first sight, there is no suggestion of a non-monotonic annular distribution as found in the Martian reanalysis. In fact, the profiles shown all have a clear polar maximum of absolute vorticity, a consequence of the thermal wind balance with the equilibrium state θ_e. However, the absolute vorticity profiles shown in Figure 1 hide one fundamental aspect, namely that, regardless of the details of the polar θ_e, the LH88 solution has a discontinuity in the wind profile at ϕ_w, a shear line with an implied δ-function of vorticity. In a viscous model, or in a model with resolved eddy mixing, such a shear line would be smoothed out over a finite latitude, with the δ-function broadening but retaining a local maximum. Thus the profiles shown do suggest that some form of annular potential vorticity distribution might arise purely as a result of the Hadley cell outflow, but to predict the detailed horizontal structure requires a model in which the transition between AMC and equilibrium regions is correctly represented. This will be addressed in the following two sections.

Before turning to the full dynamical equations, however, we note that the details of the polar vorticity depend only on the θ_e poleward of ϕ_w. Also, provided $\theta_e(\phi_w)$ itself is unchanged, the AMC winds are unaffected by changes to θ_e poleward of ϕ_w, since they are determined purely by matching conditions involving θ at the transition latitudes. Therefore, by modifying θ_e poleward of ϕ_w the polar

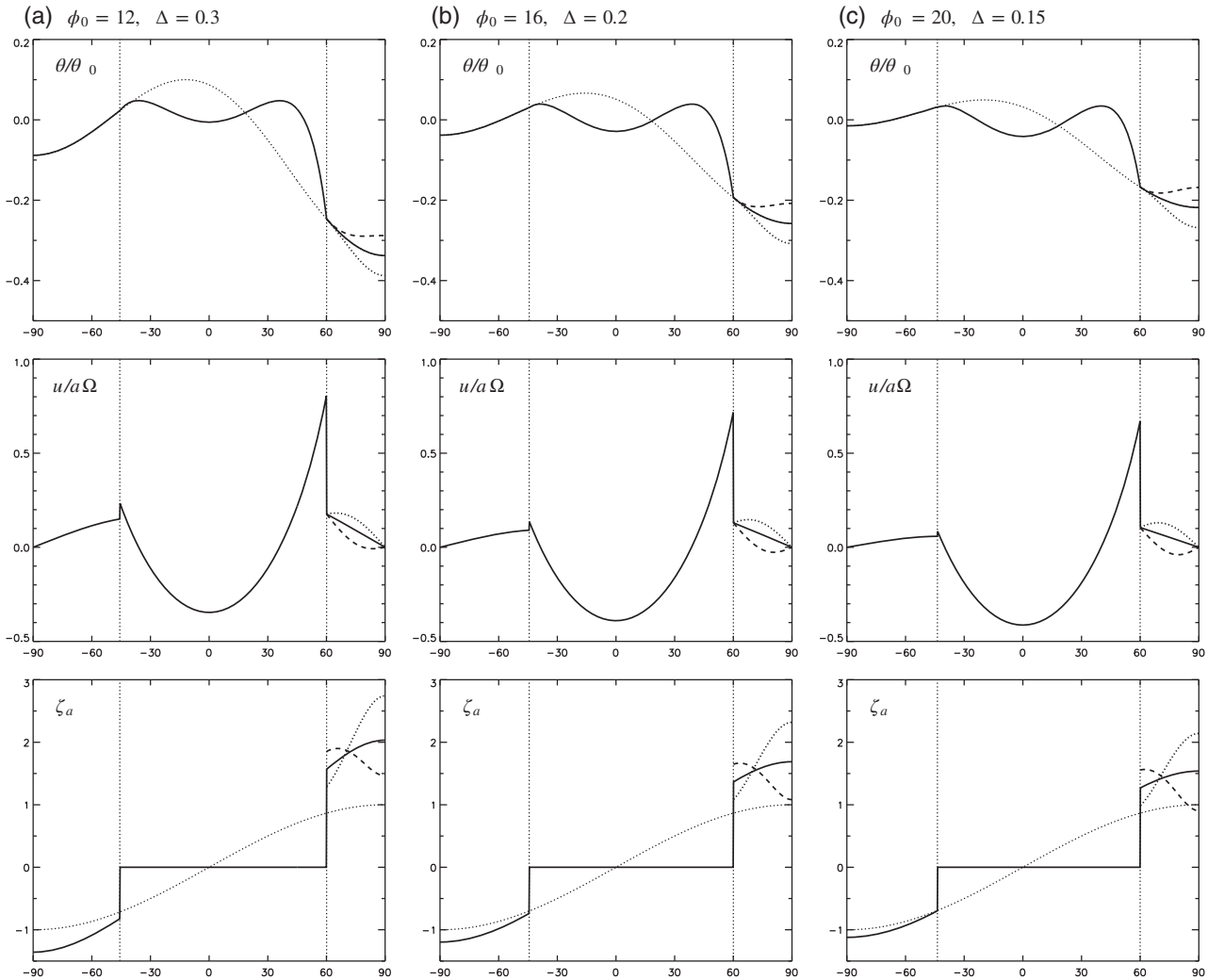

FIGURE 2 Profiles of θ/θ_0, u and ζ_a for solutions of LH88 with $\phi_w = 60°$. Vertical dotted lines indicate ϕ_w and ϕ_s. The thin dotted curves in the top panels indicate θ_e/θ_0. The dotted (dashed) curves between 60° and 90° represent the equilibrium solutions with additional polar cooling (heating)

vorticity profile can be changed directly, without altering the AMC circulation and vorticity structure south of ϕ_w.

To illustrate, we consider how the solution changes when θ_e is modified to $\theta_e + \theta_e'$, where

$$\theta_e'(\phi_c, Q) = Q\theta_0 \cos^2\left(\frac{\pi}{2}\frac{\phi - \pi/2}{\phi_c - \pi/2}\right). \tag{3}$$

Here, $Q < 0$ corresponds to an additional cooling and $Q > 0$ to a heating. With $\phi_c = \phi_w$ the modification is restricted poleward of ϕ_w. The response to the cases $Q = \pm 0.1$ are shown by dotted and dashed lines in Figure 1. Cooling the pole (lowering θ_e) causes the polar maximum in absolute vorticity to increase, along with the zonal velocity, in accordance with thermal wind balance. Conversely, warming causes a decrease in the vorticity over the pole and an increase towards ϕ_w, resulting in a clear non-monotonic profile and polar minimum, even neglecting the contribution from the shear line. The case $Q < 0$ may be thought of as a crude representation of radiative cooling in the polar night, and the case $Q > 0$ a representation of latent heat release from carbon dioxide condensation. The two effects and their interaction with the Hadley cell may therefore be considered through the response to a single forcing term in the temperature equation.

3 | FULL AXISYMMETRIC SOLUTIONS

3.1 | Convergence to the AMC solutions

Following LH88, we next compare the AMC solutions with steady solutions obtained following the time evolution of a full axisymmetric model. Whereas LH88 solve the

axisymmetric primitive equations, here we take advantage of the relatively simple vertical structure of the solutions and instead compare them with an axisymmetric shallow-water model. In this formulation, introduced by Held and Phillips (1990), the meridional component of the shallow-water velocity represents the depth-averaged meridional velocity of the Hadley cell. Thermal forcing is represented by a relaxation of the height field to a function h_{eq} which is exactly equivalent to the depth average θ_e/θ_0 of Equation 2, with the mass loss associated with this source term corresponding to a notional vertical velocity out of the layer. Our reasons for comparing the solutions with a single-layer representation rather than the full primitive equations are partly due to numerical efficiency, since in the full eddy-resolving calculations of the next section a relatively high resolution is required to capture the eddy dynamics of the annulus instability, and partly because it is desirable to use the simplest model that captures the relevant dynamical processes, in this case the lateral transport of angular momentum and the subsequent instability associated with the horizontal shear. The single-layer representation necessarily neglects details such as the return flow in the boundary layer and allows us to examine the horizontal dynamics without the added complications of baroclinic instability.

Figure 3a shows the steady-state profiles of the shallow-water zonal velocity u and the potential vorticity $q = \zeta_a/h$ obtained from time integration of the full (axisymmetric) model with relaxation to h_{eq}, where h_{eq}/H is set to the right-hand side of Equation 2, and where H is henceforth the mean layer depth. The forcing parameters ϕ_0 and Δ and the Burger number B are the same as those used in Figure 2b. A viscosity is required in the momentum equations to regularize the δ-function in ζ_a associated with the discontinuity in u of the AMC solution at ϕ_w, with various values of the viscous coefficient ν shown. The discontinuity is captured with increasing sharpness with decreasing ν, and the solutions overall appear to be converging steadily to the AMC solution. As in LH88, the location of maximum wind lies a few degrees equatorward of ϕ_w, though it appears to be converging to ϕ_w. In the AMC region, the zonal velocity is parabolic (in $\sin\phi$) and the potential vorticity converges to almost zero. Near the poles both fields attain thermal wind balance with the equilibrium h_{eq}. It is interesting to note that convergence to the AMC solutions appears to be more robust in the shallow-water model than in the primitive equations considered by LH88, another factor that favours their use here. In particular, the potential vorticity did not appear to approach zero in LH88 and the model became transient below a critical viscosity, a phenomenon argued by Schneider (1984) to be due to non-realizability of the AMC solutions.

Convergence to the AMC solutions gives confidence in the accuracy of the AMC model, but the limit $\nu \to 0$, with its discontinuity in the zonal wind, is not particularly realistic. In a full eddy-resolving model, shear instability would be expected to mix the potential vorticity and smooth the discontinuity. Viscosity can therefore be considered as a simple representation of horizontal eddy mixing, at least to the extent that eddies mix the potential vorticity downgradient. Comparison with the eddy-resolving calculations presented in section 4 suggests that a value $\nu = 10$, indicated in bold, may be an appropriate choice. With this value of ν, potential vorticity has a local maximum near 60°, which is about 50% in excess of the polar value, while there is an additional weak local maximum at the pole itself. There is the suggestion of an annular structure but no clear minimum over the pole.

3.2 | Effect of polar heating

While the LH88 h_{eq} (or θ_e) profile provides a simple representation of the seasonal asymmetry in tropical heating, it only partially represents the strong cooling of the winter polar night. The effect of changing the profile in the polar regions to include explicitly the effect of polar cooling is a straightforward consequence of thermal wind balance north of ϕ_w. Here we add an additional cooling taking the form of Equation 3 with $\phi_c = 45°$ and $Q = -0.1$, which is similar to but slightly broader than the dotted line of Figure 2b. The resulting u and q profiles are shown in Figure 3b. There is a slight increase in both the zonal velocity and the potential vorticity over the pole, including a slight increase in the maximum jet speed, in thermal wind balance with the modified h_{eq}, but there is very little change to the AMC circulation, even though the extra cooling here does extend partially into the AMC region.

Next we add an additional perturbation to h_{eq} taking the form of Equation 3 with $\phi_c = 60°$ and $Q = 0.1$ as a crude representation of the separate effect of latent heating from carbon dioxide condensation, which produces the profiles shown in Figure 3c. As with the LH88 profiles, there is a hollowing out of the vortex core, giving a more robust and distributed annular profile with a clear polar minimum, and with the degree of non-monotonicity controlled directly by the magnitude of the heating anomaly: strong heating can reduce the polar potential vorticity towards zero or even to negative values. Some amount of additional heating beyond the original LH88 profile was in all cases necessary to change the local polar maxima in potential vorticity in Figure 3a,b to a local minimum. Again the profiles south of ϕ_w are comparatively unaffected by the additional heating.

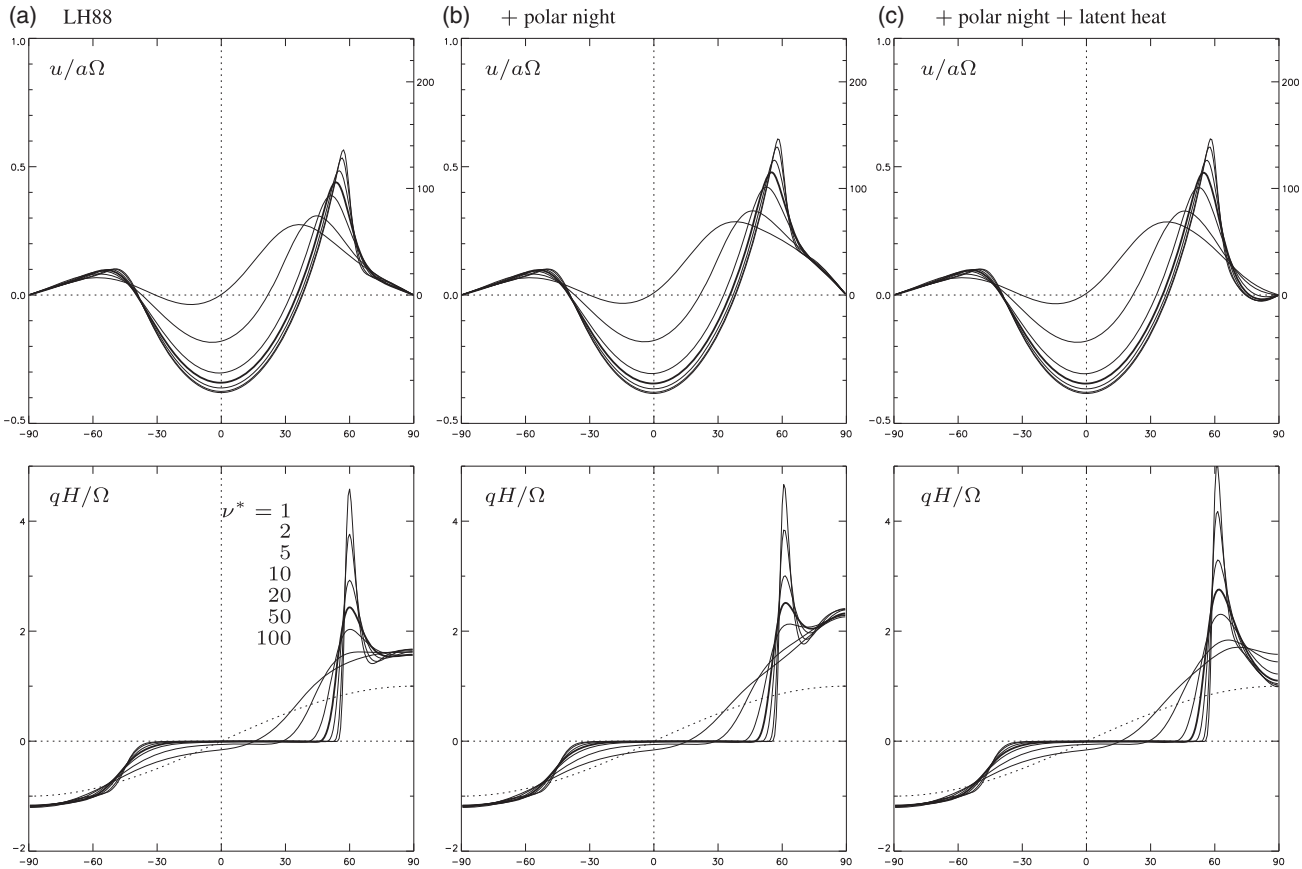

FIGURE 3 Full (axisymmetric) model solutions with parameters as in Figure 2b and diminishing viscosity, $\nu^* = \nu N(N+1)\Omega/2\pi a^2$, $N = 170$, for different choices of h_{eq}: (a) the LH88 profile; (b) the LH88 profile with enhanced polar cooling ($\phi_c = 45$, $Q = -0.1$); (c) the LH88 profile with enhanced polar cooling ($\phi_c = 45$, $Q = -0.1$) and latent heating ($\phi_c = 60$, $Q = 0.1$). The right-hand ordinates in the top panels indicate m·s^{-1}

An important point to note is that here both the additional polar cooling ($Q = -0.1$) and the polar heating ($Q = 0.1$) have the same magnitudes and cancel exactly at the pole. The differences in the thermal wind arise because we have chosen the profile of the cooling to be broader ($\phi_c = 45°$) than that of the heating ($\phi_c = 60°$). The combined perturbation has $dh_{\mathrm{eq}}/d\phi > 0$ near the Pole, corresponding to a reduced zonal wind and potential vorticity. We acknowledge that our representation of latent heating is grossly oversimplified, but the more compact distribution of latent heating is partially motivated by its dependence on extreme temperature values, compared with the broader cooling arising from the smooth latitudinal variation of insolation (Toigo *et al.*, 2017).

3.3 | Parameter dependence

Before proceeding to examine the effect of eddies on the vortex structure, it is interesting to consider briefly what can be deduced from the axisymmetric model in parameter ranges beyond those relevant for Mars. As noted above, the LH88 solutions are determined completely by two parameters: the asymmetry ϕ_0 and the combination $R = B\Delta$, where $B = gH/a^2\Omega^2$ is a planetary Burger number. Planetary parameters such as rotation and stratification therefore affect the solution only by modifying the effective heating amplitude R. The dependence of the solution on planetary parameters is essentially the same as that noted recently by Guendelman and Kaspi (2018) in terms of a thermal Rossby number proportional to R.

As seen in Figure 3, the axisymmetric solutions depend strongly on viscosity. To be useful, therefore, an estimate must be made of appropriate eddy viscosity values, and as noted above, comparison with the eddy-resolving calculations presented in the next section suggests a value $\nu = 10$. Using this value, the axisymmetric model provides a crude but quick estimate of the possible atmospheric regimes that may arise under different planetary parameters. Fixing the heating and varying ϕ_0, for example, produces the profiles shown in Figure 4a, which gives an indication of the range of Hadley cell and polar vortex strengths that

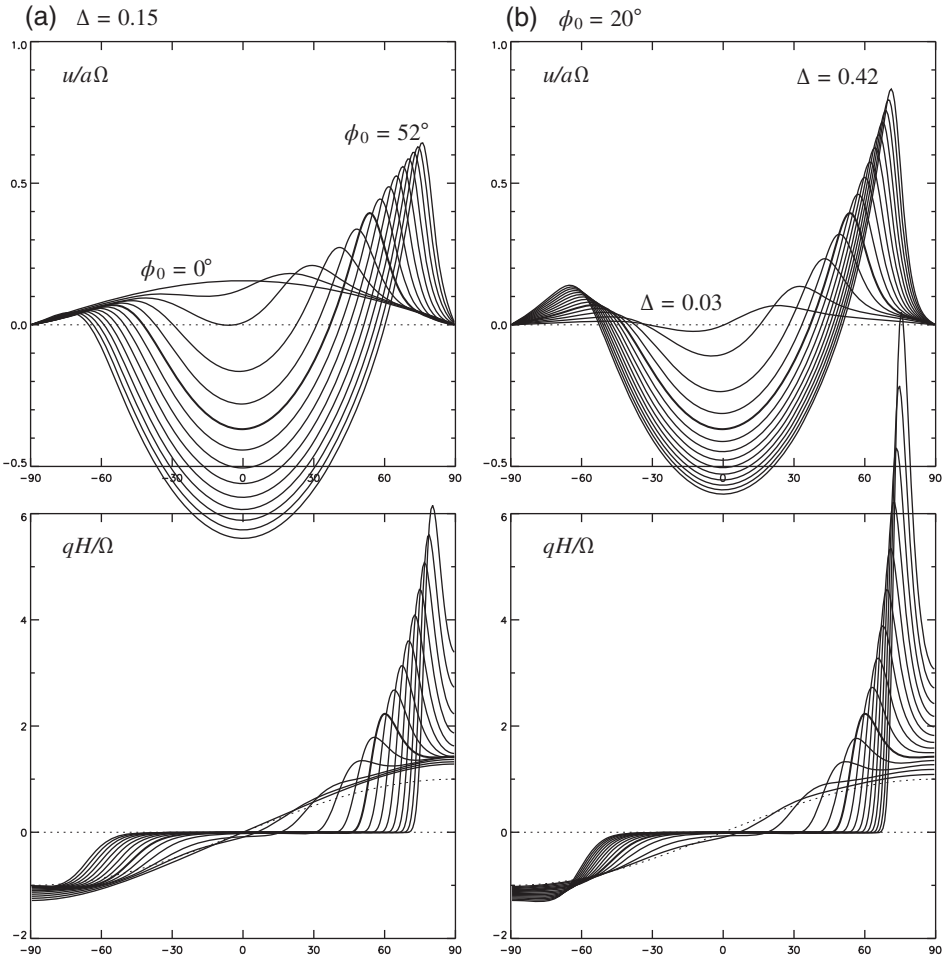

FIGURE 4 Full (axisymmetric) model solutions with LH88 heating and $\nu = 10$. (a) Fixed $\Delta = 0.15$, ϕ_0 ranging from 0° to 52° in steps of 4°. (b) Fixed $\phi_0 = 20°$, Δ ranging from 0.03 to 0.42 in steps of 0.03

might have existed on Mars during periods when the planetary obliquity was substantially different from its current value.

Alternatively, for fixed obliquity, the range of possible circulations that might be obtained with different heating strengths is shown in Figure 4b. In these calculations, B is fixed at the same (Martian) value used above, but the same plot would be obtained by fixing Δ and varying B such that $R = B\Delta$ varies over the corresponding range. This makes explicit how the Hadley cell extent is expected to vary with, say, planetary rotation, all other parameters being equal: a lower rotation rate implying larger B, hence larger R and a stronger Hadley cell and a more poleward polar vortex. Similarly, at a fixed rotation, stronger stratification would again imply a stronger Hadley cell. As pointed out by Guendelman and Kaspi (2018), of the physical parameters that appear in B, it is the rotation rate that shows the largest variation in relative values, at least among Solar System planets.

Of course, some caution is required in interpreting such crude estimates; for instance, the assumed value of eddy viscosity used here is based on the eddy-resolving simulations below and it may not be the most appropriate choice for other regimes, since eddy length scales will also depend on B (Walker and Scheider, 2006). Nonetheless, the above results are consistent with studies in which full general circulation models have been used to estimate the dependence of the Hadley cell structure on different planetary parameters. For example, the recent study of Guendelman and Kaspi (2019) found that the Hadley cell width increased with increasing obliquity (increasing ϕ_0) and decreasing rotation rate (increasing B), as in Figure 4.

4 | COMPARISON WITH AN EDDY-RESOLVING MODEL

4.1 | Model details

We next consider the extent to which the axisymmetric annular structure obtained above persists in a full, eddy-resolving shallow-water model, where the growth of eddies from shear instability is represented. The model equations and physical constants are exactly as described in Seviour *et al.* (2017) (eqs. 1a–c therein) but with no

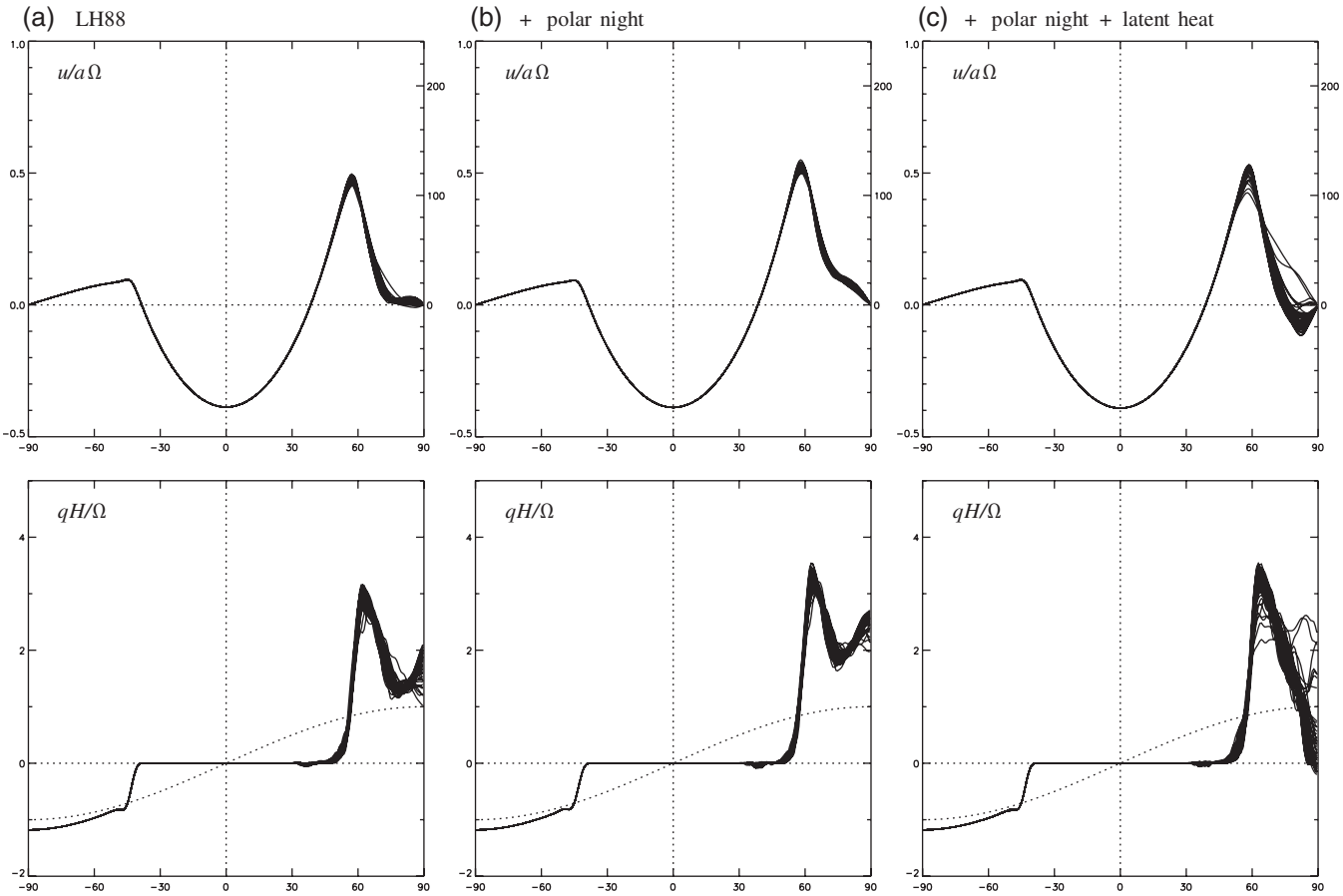

FIGURE 5 Full eddy-resolving model zonal mean fields with parameters as in Figure 3. Lines are separated by 10 sol intervals between $t = 1,500$ and $t = 2,000$. Units for u: $a\Omega$ (left axis), $\mathrm{m{\cdot}s^{-1}}$ (right axis). Units for q: 2Ω. Equilibrium h_{eq}: (a) LH88 profile; (b) LH88 profile with enhanced polar cooling ($\phi_c = 45$, $Q = -0.1$); (c) LH88 profile with enhanced polar cooling ($\phi_c = 45$, $Q = -0.1$) and latent heating ($\phi_c = 60$, $Q = 0.1$)

topography, $h_b \equiv 0$, and solved by the same pseudospectral method with triangular truncation at the total wavenumber 170 (T170). We consider the "inviscid limit" in the sense that the viscosity is set to zero, although the model uses a fourth-order hyperdiffusion for numerical stability; however, at all but the smallest scales the hyperdiffusion is much less dissipative than the second-order viscosity used above. The equilibrium height h_{eq} is as used in section 3, namely the LH88 profile with various combinations of additional polar cooling and heating. The relaxation time-scale τ_{rad} is set to 1 sol in most of the experiments, again following Seviour *et al.* (2017) and as suggested by Eckermann *et al.* (2011), with the dependence on this parameter examined in section 4.4 below. A natural extension not considered here would be to allow the polar heating to depend interactively on the height field, mimicking the dependence of carbon dioxide condensation on temperature, in a manner similar to that considered recently by Rostami *et al.* (2018).

4.2 | Influence of polar heating

Figure 5 shows the zonal mean zonal velocity and potential vorticity profiles for the same combinations of heating as used in the axisymmetric calculations shown in Figure 3. Eddies are not explicitly forced in these calculations, but develop from the shear instability associated with the polar potential vorticity distribution. Consequently, the flow does not reach a steady state but it does reach a statistical equilibrium on time-scales of a few hundred sols. The profiles in Figure 5 are plotted at 10 sol intervals over the time period $t = 1,500$ to $t = 2,000$ sols, which gives an idea of the average profile over that period as well as the degree of transience due to the eddy evolution.

Comparing with Figure 5, it is seen that the zonal mean evolution states of the full shallow-water model are quite similar to the axisymmetric solutions with the value $\nu = 10$. In particular, in all cases there is a distinct potential vorticity maximum near 60°N and associated jet maximum,

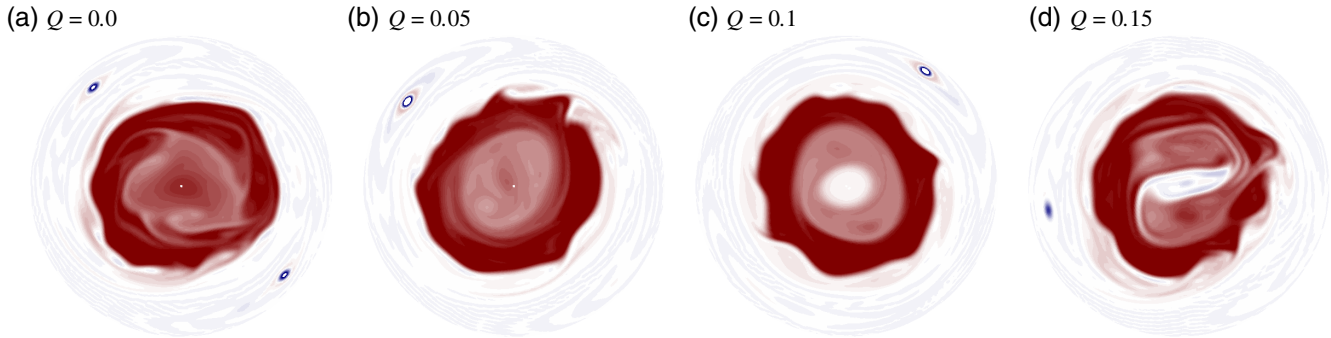

FIGURE 6 Potential vorticity at $t = 2,000$ sols for simulations with latent heating values $Q = 0, 0.05, 0.1, 0.15$ (a–d). Cases (a) and (c) correspond to the simulations shown respectively in Figure 5b,c [Colour figure can be viewed at wileyonlinelibrary.com]

resulting from angular momentum transport from lower latitudes in an AMC circulation. Again, the potential vorticity is almost exactly zero over most of the AMC region. Poleward of 60°N, the flow is determined by the details of the additional polar cooling or heating. Only with additional heating over the pole is a distinct polar potential vorticity minimum obtained. In all cases, the relatively small spread of individual lines indicates that the zonal mean flow is persistent in time, despite the instability associated with the non-monotonic potential vorticity. The biggest variations are found in the case with latent heating, where a few individual profiles indicate infrequent but substantial disruptions to the annulus. These are considered in more detail in what follows.

Snapshots of the potential vorticity at $t = 2,000$ sols from four integrations with different values of heating $Q = 0, 0.05, 0.1, 0.15$ in Equation 3 are shown in Figure 6a–d, illustrating the effect of increasing latent heating on both the annular structure and the eddy field. The case $Q = 0$ corresponds to Figure 5a, while $Q = 0.1$ corresponds to Figure 5c. The influence of latent heat is visible in the core, with a deepening potential vorticity minimum for increasing Q.

At first sight, the pattern of eddy activity visible in Figure 6 is somewhat surprising, with the case $Q = 0.1$ exhibiting the most zonally symmetric annulus of the four, despite having a greater degree of potential vorticity gradient reversal poleward of the jet than the cases $Q = 0$ and $Q = 0.05$, corresponding to a more unstable vortex. It turns out that the anomaly is due to the transient nature of the evolution. This can be illustrated by considering the integrated eddy enstrophy, defined as

$$Z = \frac{1}{4\pi} \int q'^2 dA, \tag{4}$$

where $q' = q - \overline{q}$ is the departure from the zonal mean potential vorticity. The eddy enstrophy, Z, is shown in Figure 7 for the cases $Q = 0$, $Q = 0.1$ and $Q = 0.15$ (the case $Q = 0.05$ is similar to $Q = 0$) over the time period $t = 1,500$ to $t = 2,000$ sols. First, there is a small but definite increase in the mean enstrophy with increasing Q (time-averaged values of Z are 0.64, 0.69, 0.72 and 0.89, respectively), indicating an overall increase in the eddy activity as the polar potential vorticity minimum deepens, in line with expectations from basic stability considerations. Moreover, there is a substantial increase in the variance of eddy enstrophy, indicating greater transience in the flow at larger Q. In all cases, the time evolution takes the form of quasi-regular vacillations with a characteristic period of about 20–40 sols that decreases with increasing Q, while the amplitude increases. The strong annularity of the vortex in the case $Q = 0.1$ shown in Figure 6c is thus associated with the minimum in Z at $t = 2,000$ in Figure 7b. Similarly, the relatively wavy vortex in the case $Q = 0$ (Figure 6a) corresponds to a local maximum in Z at $t = 2,000$ (Figure 7a).

The evolution of the vortex during the course of a typical vacillation cycle is shown in Figure 8. The plot shows polar potential vorticity at 2 and 4 sol intervals between $t = 1,890$ and $t = 1,904$, while the corresponding eddy enstrophy can be seen in Figure 7b. At the beginning of this period the polar annulus is well formed and almost completely zonally symmetric, with some weak filamentary structure near the innermost edge remaining from mixing during the previous cycle. Over the next 4 sols a strong wavenumber 3 disturbance grows on the inner edge, and subsequently strengthens to the extent that it causes considerable mixing over a region that gradually encroaches deeper into the annulus core ($t = 1,900$). Towards the end of the period shown, most of the eddy enstrophy has been dissipated by strong mixing within the annulus and potential vorticity gradients in the interior are reduced overall. The transience found here is reminiscent of, but on shorter time-scales than, vacillation cycles identified in simplified models of the Earth's winter stratospheric polar vortex (e.g., Scott, 2016), where the vortex is monopolar and shear stable, and the disturbances are forced through

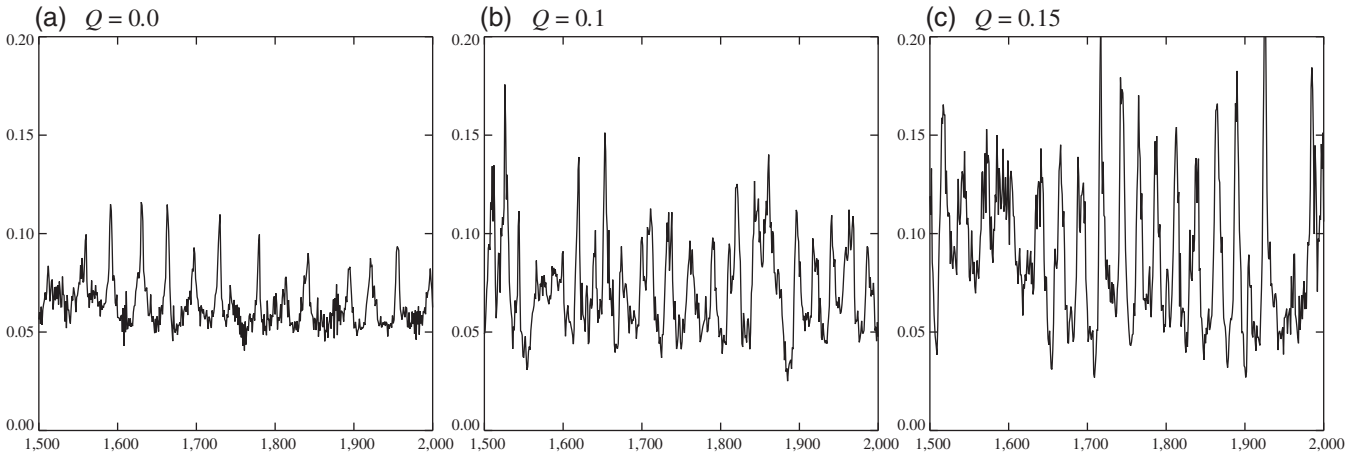

FIGURE 7 Evolution of eddy enstrophy for the cases $Q = 0, 0.1, 0.15$ (a–c)

planetary wave excitation from the troposphere below. A closer analogy may be found in the rotating annulus experiments of, for example, Young (2014). The cycle shown in Figure 7 is typical of the annulus evolution between peaks in the eddy enstrophy.

A more extreme example is shown in Figure 9 for the case $Q = 0.15$ over similarly spaced time intervals between $t = 1{,}922$ and $t = 1{,}936$. Again, a wavenumber 3 disturbance grows initially on the inner edge, but in this case it grows to sufficiently large amplitudes that the entire annulus is distorted and eventually breaks up completely. Over the next few sols, air is mixed vigorously over the entire polar cap, weakening the maximum potential vorticity values. The annular structure is only gradually recovered from about $t = 1,940$ (not shown).

An examination of potential vorticity maps from both the Mars Analysis Correction Data Assimilation (MACDA v1.0) (Montabone *et al.*, 2014) and the Ensemble Mars Atmosphere Reanalysis System (EMARS) (Greybush *et al.*, 2012) reveals a certain amount of variability in the Martian polar annulus not dissimilar to that presented here (see, e.g., Waugh *et al.*, 2016, their fig. 12). A detailed comparison is complicated in part by the presence of strong topographic variations on Mars, which provide a wave forcing to the annulus that is absent in the model integrations. Transience in the observed wavenumber 3 can be found, as in Figure 8, but the evolution likely involves interactions between unstable eddy growth and the fixed topographic forcing. The lower resolution of the reanalysis also makes it harder to follow the Lagrangian evolution of air masses and the details of the potential vorticity mixing. As the reanalysis improves, we anticipate that a more careful study of transience will be useful, possibly involving a decomposition into distinct zonal wavenumbers to separate transience due to unstable growth from that due to topographic interactions.

For completeness, we note that all of the four cases considered in Figure 6 exhibit one or two strong compact anticyclones at lower latitudes, around 30°N, in the region of near-zero potential vorticity in the AMC region. At first these were thought to be numerical artefacts, possibly arising from overshoots associated with the hyperdiffusion. Further integrations have been carried out at various resolutions and with different forms of small-scale diffusion, including ordinary viscosity. In all cases, similar anticyclones were obtained and these appear to be properly resolved dynamical features. They develop at early times in the model evolution, at the onset of the first instability of the shear zone at the edge of the AMC region, and appear to arise from the interaction of the wave breaking with the strong relaxation on the height field. Once formed, they persist largely independently of the flow at high latitudes. Because they are comparatively small-scale features, their influence on the polar dynamics is presumably weak; their scale in relation to the main polar vortex can be inferred from the small dip in zonal mean profiles in Figure 5. While interesting, and possibly important for the dynamics at lower latitudes, they fall outside of the scope of the present work and will not be investigated further here.

4.3 | Influence of the Hadley cell

As discussed in section 2, different combinations of heating asymmetry and heating magnitude can combine to produce the same edge ϕ_w of the AMC region. The AMC solutions for the three particular choices ($\phi_0 = 12, \Delta = 0.3$), ($\phi_0 = 16, \Delta = 0.3$) and ($\phi_0 = 20, \Delta = 0.15$) were shown in Figure 2. We ran the full eddy-resolving model with the same parameters, with enhanced polar cooling as above, with and without additional polar latent

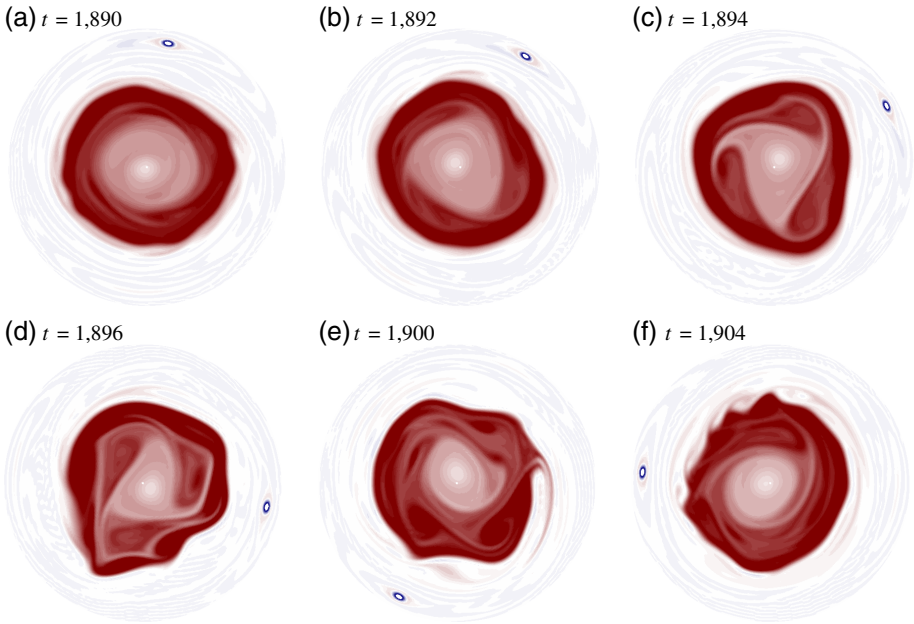

FIGURE 8 Potential vorticity for the case $Q = 0.1$ at times between $t = 1{,}890$ and $t = 1{,}904$ (a–f) [Colour figure can be viewed at wileyonlinelibrary.com]

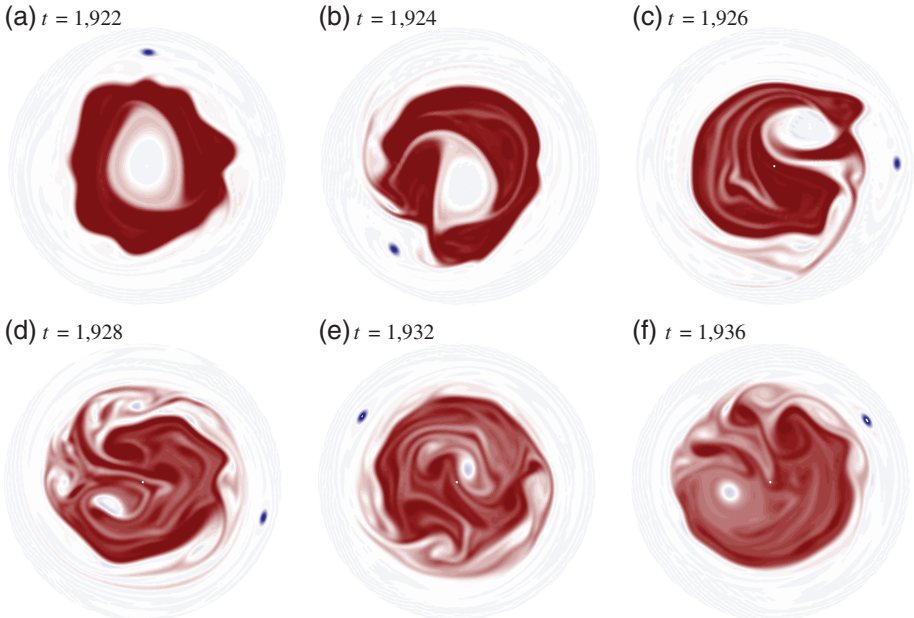

FIGURE 9 Potential vorticity for the case $Q = 0.15$ at times between $t = 1{,}922$ and $t = 1{,}936$ (a–f) [Colour figure can be viewed at wileyonlinelibrary.com]

heating. The zonal mean zonal velocity and potential vorticity profiles are shown in Figure 10, where the profiles have been averaged in time from $t = 700$ to $t = 1{,}000$ for clarity.

The dependence of the AMC flow on ϕ_0 is similar to the solutions shown in Figure 2, with slightly higher zonal velocity values across the tropics for $\phi_0 = 12$, decreasing with ϕ_0, regardless of the details of the polar heating. The zonal velocity at the vortex edge shows a similar dependence, as does the peak potential vorticity. The differences are relatively small compared with the two-fold change in the pole-to-equator equilibrium height difference across this range of Δ.

To measure the extent to which the peak potential vorticity values at ϕ_w influence the stability of the vortex, we again consider the eddy enstrophy as defined by Equation 4. For the three cases with polar heating shown in Figure 10b, we show in Figure 11 the integrated eddy enstrophy as a function of time. The case $\phi_0 = 16$ has been repeated for easy reference. Eddy enstrophy is largest for the case $\phi_0 = 12$, consistent with the higher peak potential vorticity of the annulus in that case, and decreases with increasing ϕ_0: time-mean values over the period shown are 0.102, 0.072 and 0.058, respectively. Aside from the decrease in mean values, the variance and characteristic time-scales of the variability are broadly similar across

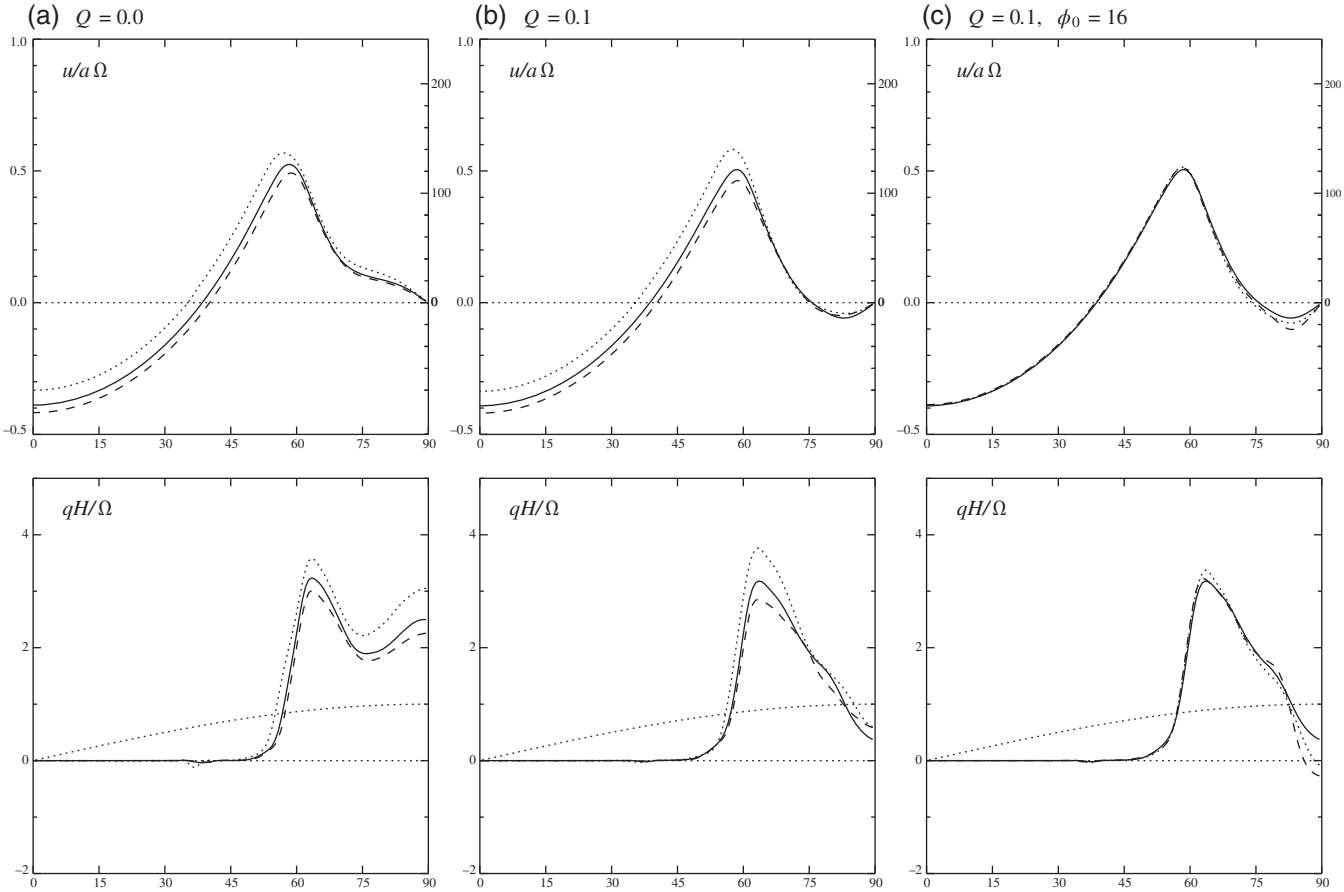

FIGURE 10 (a,b) Time-averaged (1,500–2,000 sol) zonal mean zonal velocity and potential vorticity profiles for cases with Hadley cell forcing $\phi_0 = 12$S, $\Delta = 0.3$ (dotted lines); $\phi_0 = 16$S, $\Delta = 0.2$ (solid lines) and $\phi_0 = 20$S, $\Delta = 0.15$ (dashed lines): (a) with no latent heating and (b) with latent heating ($Q = 0.1$). Panel (c) shows the corresponding quantities for the case $\phi_0 = 16$S, $\Delta = 0.2$ with latent heating, and for values of $\tau_{\rm rad} = 0.5$ (dotted line) and $\tau_{\rm rad} = 2$ (dashed line), with the case $\tau_{\rm rad} = 1$ (solid line) shown again for comparison

the three cases. Clear vacillation cycles occur in all cases, exhibiting somewhat less regularity with increasing ϕ_0, at least over the time interval shown.

4.4 | Influence of the radiative time-scale

Finally we consider briefly the effect of $\tau_{\rm rad}$ on the eddy evolution of the annulus. On Mars, the radiative time-scale is short and tightly controls the thermal wind solution poleward of ϕ_w. However, the Hadley cell itself is established on much longer time-scales, typically of the order of 500 sols for the cases discussed above. While we expect the radiative time-scale to affect the polar dynamics in a manner similar to that discussed in Seviour *et al.* (2017), such as weaker annular stability at larger $\tau_{\rm rad}$, it is possible that differences may arise due to the way in which the Hadley cell forces the potential vorticity structure on longer time-scales. We therefore consider two further simulations in which the value of $\tau_{\rm rad} = 1$ sol used in the previous section was increased or decreased by a factor of two, keeping all other parameters fixed.[1]

The zonal mean zonal velocity and potential vorticity profiles for the range of $\tau_{\rm rad}$ are shown in Figure 10c. Both cases, $\tau_{\rm rad} = 0.5$ (dotted line) and $\tau_{\rm rad} = 2$ (dashed line), are almost identical to the case $\tau_{\rm rad} = 1$ (solid line) previously examined, except very close to the pole, where there are small variations in the minimum potential vorticity attained. Care has been taken in all cases to ensure that the averaging period lies well after the flow has reached a statistically stationary state.

The eddy enstrophy for each simulation is shown in Figure 12, where again the case $\tau_{\rm rad} = 1$ has been repeated for easy reference. Fluctuations in the eddy enstrophy

[1]Because the representation of latent heating in our model is through a modification of θ_e, changing $\tau_{\rm rad}$ changes the absolute heating associated with this modification. To keep the absolute latent heating fixed would require θ_e' to vary inversely with $\tau_{\rm rad}$, changing the equilibrium state and resulting in a large dependence of the polar state on the $\tau_{\rm rad}$. Here we are only interested in the effect of $\tau_{\rm rad}$, keeping θ_e fixed.

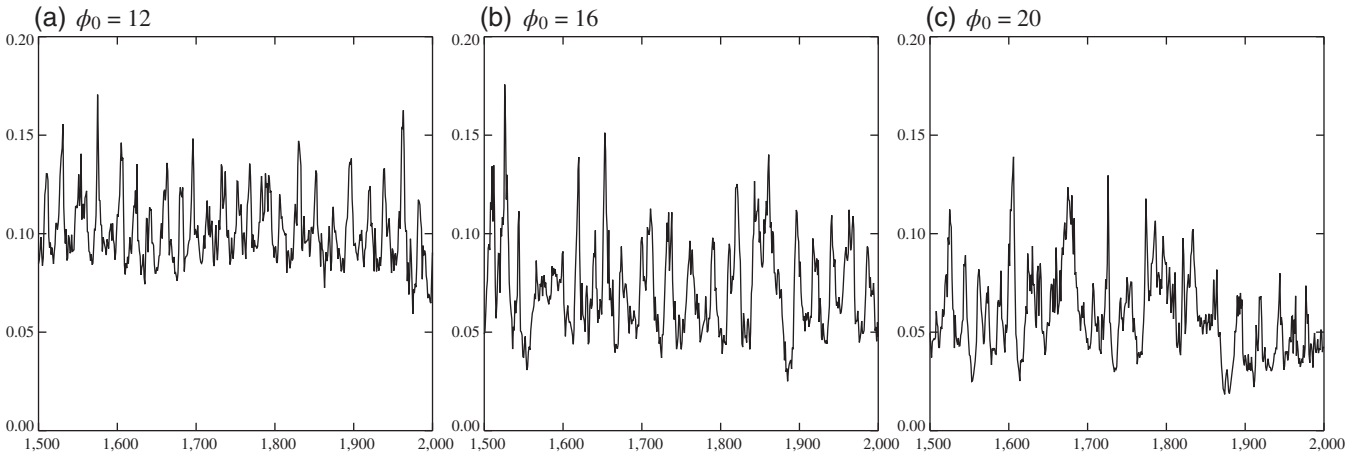

FIGURE 11 Eddy enstrophy evolution for the three cases shown in Figure 10b

again take the form of quasi-regular vacillation cycles, with the characteristic period decreasing with τ_{rad} from about 50 sols at $\tau_{\text{rad}} = 2$ to about 20 sols at $\tau_{\text{rad}} = 0.5$. In all cases the characteristic period is very short compared with the time-scale for equilibration, but very long compared with the radiative time-scale.

Perhaps surprisingly, the mean eddy enstrophy increases with decreasing τ_{rad}. It might be expected that the stronger relaxation over the pole would keep the potential vorticity more tightly constrained in a zonally symmetric annular form. However, it should be remembered that the annular structure here is generated indirectly through the Hadley cell forcing, rather than by direct radiative forcing (again, the main difference between the current formulation and that of Seviour *et al.* (2017)). Aside from the increase in the mean, the amplitudes of the cycles (peak-to-peak change) are not strongly dependent on τ_{rad}.

Other differences in the character of the vacillations can be seen upon closer comparison of the $\tau_{\text{rad}} = 2$ and $\tau_{\text{rad}} = 0.5$ cases. The longer period at $\tau_{\text{rad}} = 2$, for example, appears to be associated with a slower increase in eddy enstrophy towards the peak, with the suggestion of a sawtooth shape in the interval $t = 1{,}600$–$1{,}800$. In these cases the recovery to annular form occurs relatively quickly. Thus it appears that the variation in the period with τ_{rad} is more than a simple linear response to the relaxation time-scale. To illustrate the difference, four snapshots of the polar potential vorticity from each of the cases $\tau_{\text{rad}} = 2$ and $\tau_{\text{rad}} = 0.5$ are shown in Figure 13. For $\tau_{\text{rad}} = 2$ (panels a–d; note that the panels are at 12 sol intervals), there is a relatively slow increase in wave amplitude from the minimum near $t = 1,712$ to the maximum near $t = 1,748$, and a correspondingly gradual increase in the potential vorticity mixing in the annulus. In contrast, for $\tau_{\text{rad}} = 0.5$ (panels e–h; note that the panels are now at 2 sol intervals), the distortion of the annulus occurs much more rapidly, with strong mixing taking place just 6 sols after the minimum. The more rapid development of the instability in the latter case cannot be attributed to a direct effect of the shorter radiative time-scale, but must arise indirectly through the influence of the zonal mean annular structure on unstable growth rates. It should be noted, however, that such behaviour is by no means universal; all three time series exhibit significant irregularities, and examples of rapid eddy growth also exist at $\tau_{\text{rad}} = 2$ (e.g., $t = 1{,}900$).

5 | CONCLUSIONS

We have shown that the annular potential vorticity structure of the Martian polar vortex arises naturally from the combination of two basic forcing mechanisms: an angular momentum conserving (AMC) Hadley cell driven by off-equatorial heating, and enhanced heating over the winter pole representing the latent heat release from carbon dioxide condensation. The simplified AMC Hadley cell model of Lindzen and Hou (LH88) is capable of capturing the Martian circulation even though the winter branch of the Hadley cell extends much further north than on Earth. The model allows the dependence of the polar potential vorticity distribution on each aspect of the forcing to be examined in a clear and unambiguous way. In particular, the location of the zonal wind maximum is controlled mainly by the asymmetry and forcing strength of the Hadley cell, while the details of the flow poleward of the jet are controlled mainly by details of the equilibrium temperature field in that region through thermal wind balance.

While the potential vorticity structure of the LH88 model shows no explicit annular structure, the infinite shear at the transition latitude implies a δ-function

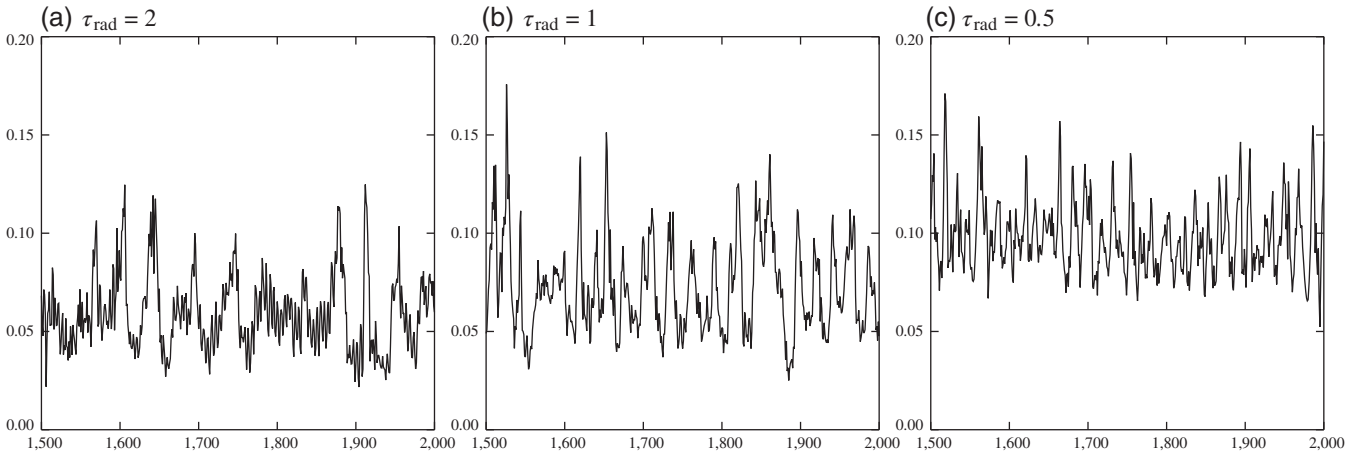

FIGURE 12 Eddy enstrophy evolution for the three cases shown in Figure 10c: (a) $\tau_{rad} = 2$, (b) $\tau_{rad} = 1$ and (c) $\tau_{rad} = 0.5$. In all cases $\phi_0 = 16$ and $Q = 0.1$

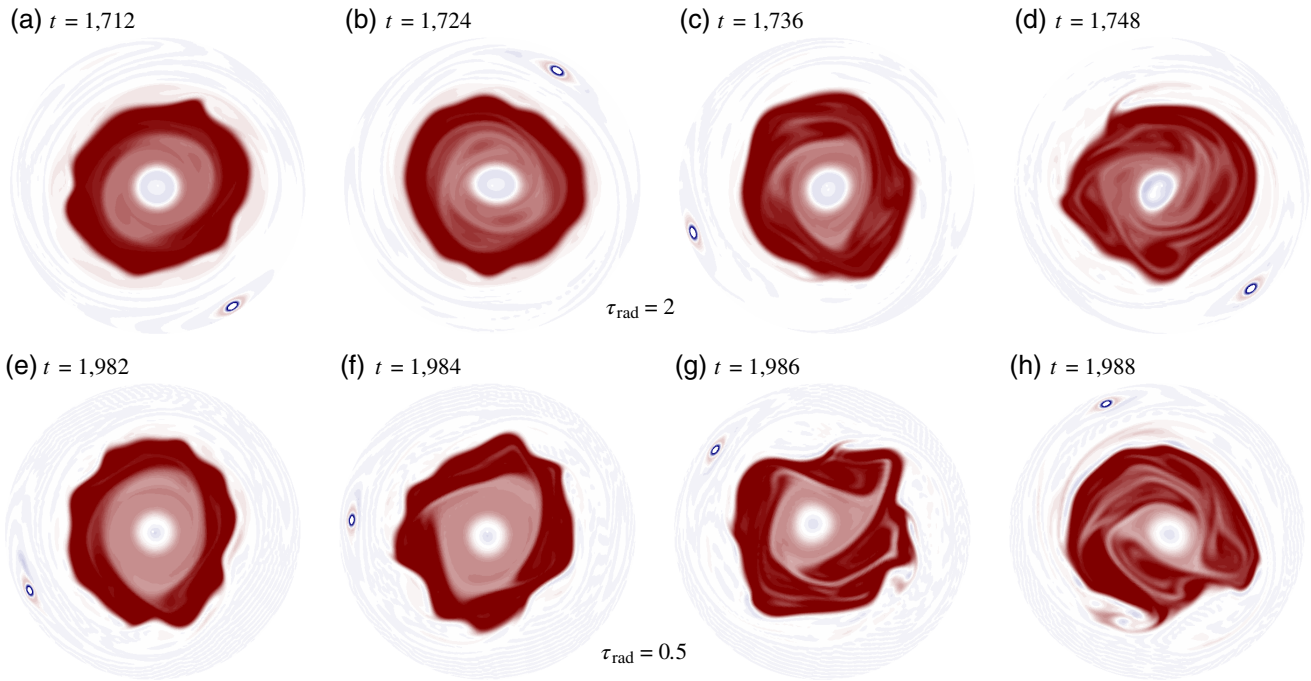

FIGURE 13 Potential vorticity from simulations with $\tau_{rad} = 2$ (a–d), corresponding to Figure 12a, and $\tau_{rad} = 0.5$ (e–h), corresponding to Figure 12c, at selected representative times [Colour figure can be viewed at wileyonlinelibrary.com]

in vorticity that could lead to a local maximum when smoothed by viscosity or eddy mixing in a full model. However, when the latter effects are included, although a potential vorticity maximum is produced near 60°N, there is also a weaker but well-defined local maximum over the pole. This local polar maximum is stronger when a representation of the enhanced cooling of the polar night is included. To obtain a distinct polar minimum, on the other hand, some additional heating is required, with the depth of the minimum increasing with increasing heating strength. The result is consistent with the general circulation model (GCM) experiment of Toigo *et al.* (2017), which found that a monopolar vortex developed when the parametrization of latent heating from carbon dioxide condensation was switched off, although in our model some degree of annular structure does arise from the Hadley cell alone. The Hadley cell itself imposes a robust constraint on the location of the maximum of the potential vorticity through the determination of the latitude ϕ_w.

In a full, non-axisymmetric shallow-water model with resolved eddies, the basic dependence on Hadley cell and additional polar heating was confirmed. In this model,

with a radiative relaxation time-scale of 1 sol, a stationary state was established on time-scales of a few hundred sols, suggesting that the final states are attainable on time-scales of the Martian seasonal cycle. Despite the transience associated with the nonlinear eddy evolution arising from shear instability of the annulus, the basic annular structure persists in the time mean. Typically, eddy amplitudes were found to grow over time-scales of a few sols, saturate and then cause transient mixing of the annular structure. When the eddies are strained to small scales and dissipated, the annulus is able to re-form under the action of the direct radiative forcing to the thermal wind in the polar regions, giving rise to vacillation cycles on time-scales of a few tens of sols. The amplitude of these cycles increases as the additional polar heating is increased, to the point where the vacillations can result in complete mixing of the annulus across the polar region. Although the vacillation time-scale increases with radiative time-scale, the dependence does not appear to be linked to a direct change in the restoration time-scale of the annulus under radiative forcing, but rather to changes in the growth rate of the eddy activity.

Aside from elucidating the mechanisms that control the annular structure, as discussed in section 3.3, the axisymmetric model provides a quick way of exploring possible circulation patterns that may exist on other planets. In particular, the AMC model formulation depends explicitly on only two parameters: the latitude of the off-equatorial heating maximum and the effective heating strength. The latter is a combination of the actual pole-to-equator equilibrium temperature difference multiplied by a planetary Burger number that measures the relative importance of rotation and stratification. Thus, low rotation or high stratification is associated with higher effective heating strength and a wider Hadley cell. While more detailed aspects of the dynamics will depend on individual physical parameters, the above suggests that when conducting parameter sweep experiments of possible circulation regimes in exo-planetary atmospheres, the effects of solar luminosity, planetary mass, rotation, etc., should initially be considered in combination.

ORCID

R. K. Scott https://orcid.org/0000-0001-5624-5128

REFERENCES

Banfield, D., Conrath, B., Gierasch, P., John Wilson, R. and Smith, M. (2004) Traveling waves in the martian atmosphere from MGS TES nadir data. *Icarus*, 170, 365–403

Barnes, J.R. and Haberle, R.M. (1996) The Martian zonal-mean circulation: angular momentum and potential vorticity structure in GCM simulations. *Journal of the Atmospheric Sciences*, 53, 3143–3156

Broyden, C.G. (1965) A class of methods for solving nonlinear simultaneous equations. *Mathematics of Computation*, 19, 577–593

Dritschel, D.G. and Polvani, L.M. (1992) The roll-up of vorticity strips on the surface of a sphere. *Journal of Fluid Mechanics*, 234, 47–69

Eckermann, S.D., Ma, J. and Zhu, X. (2011) Scale-dependent infrared radiative damping rates on Mars and their role in the deposition of gravity-wave momentum flux. *Icarus*, 211, 429–442

Greybush, S.J., Wilson, R.J., Hoffman, R.N., Hoffman, M.J., Miyoshi, T., Ide, K., McConnochie, T. and Kalnay, E. (2012) Ensemble Kalman filter data assimilation of Thermal Emission Spectrometer temperature retrievals into a Mars GCM. *Journal of Geophysical Research*, 117, E11008

Guendelman, I. and Kaspi, Y. (2018) An axisymmetric limit for the width of the Hadley cell on planets with large obliquity and long seasonality. *Geophysical Research Letters*, 45, 13213–13221

Guendelman, I. and Kaspi, Y. (2019) Atmospheric dynamics on terrestrial planets: the seasonal response to changes in orbital, rotational, and radiative timescales. *The Astrophysical Journal*, 881, 67

Held, I.M. and Hou, A.Y. (1980) Nonlinear axially symmetric circulations in a nearly inviscid atmosphere. *Journal of the Atmospheric Sciences*, 37, 515–533

Held, I.M. and Phillips, P.J. (1990) A barotropic model of the interaction between the Hadley cell and a Rossby wave. *Journal of the Atmospheric Sciences*, 47, 856–869

Hide, R. (1969) Dynamics of the atmospheres of the major planets with an appendix on the viscous boundary layer at the rigid bounding surface of an electrically-conducting rotating fluid in the presence of a magnetic field. *Journal of the Atmospheric Sciences*, 26, 841–853

Leovy, C. (2001) Weather and climate on Mars. *Nature*, 412, 245–249

Lindzen, R.S. and Hou, A.Y. (1988) Hadley circulations for zonally averaged heating centered off the equator. *Journal of the Atmospheric Sciences*, 45, 2416–2427

McConnochie, T.H. (2007). Observations of the Martian atmosphere: THEMIS-VIS calibration, mesospheric clouds, and the polar vortex. Ph.D. thesis, Cornell University. https://ecommons.cornell.edu/handle/1813/3517.

Mitchell, D.M., Montabone, L., Thomson, S. and Read, P.L. (2015) Polar vortices on Earth and Mars: a comparative study of the climatology and variability from reanalyses. *Quarterly Journal of the Royal Meteorological Society*, 141, 550–562

Montabone, L., Lewis, S., Read, P. and Hinson, D. (2006) Validation of Martian meteorological data assimilation for MGS/TES using radio occultation measurements. *Icarus*, 185, 113–132

Montabone, L., Marsh, K., Lewis, S.R., Read, P.L., Smith, M.D., Holmes, J., Spiga, A., Lowe, D. and Pamment, A. (2014) The Mars Analysis Correction Data Assimilation (MACDA) dataset v1.0. *Geoscience Data Journal*, 1, 129–139

Richardson, M.I. and Wilson, R.J. (2002) A topographically forced asymmetry in the Martian circulation and climate. *Nature*, 416, 298–301

Rostami, M., Zeitlin, V. and Montabone, L. (2018) On the role of spatially inhomogeneous diabatic effects upon the evolution of Mars' annular polar vortex. *Icarus*, 314, 376–388

Schneider, E.K. (1983) Martian great dust storms: interpretive axially symmetric models. *Icarus*, 55, 302–331

Schneider, E.K. (1984) Response of the annual and zonal mean winds and temperatures to variations in the heat and momentum sources. *Journal of the Atmospheric Sciences*, 41, 1093–1115

Scott, R.K. (2016) A new class of vacillations of the stratospheric polar vortex. *Quarterly Journal of the Royal Meteorological Society*, 142, 1948–1957

Seviour, W.J.M., Waugh, D.W. and Scott, R.K. (2017) The stability of Mars' annular polar vortex. *Journal of the Atmospheric Sciences*, 75, 1533–1547

Toigo, A.D., Waugh, D.W. and Guzewich, S.D. (2017) What causes Mars' annular polar vortices?. *Geophysical Research Letters*, 44, 71–78

Walker, C.C. and Scheider, T.S. (2006) Eddy influences on Hadley circulations: simulations with an idealized GCM. *Journal of the Atmospheric Sciences*, 63, 3333–3350

Waugh, D.W. and Dritschel, D.G. (1991) The stability of filamentary vorticity in two-dimensional geophysical vortex-dynamics models. *Journal of Fluid Mechanics*, 231, 575–598

Waugh, D.W., Toigo, A.D., Guzewich, S.D., Greybush, S.J., Wilson, R.J. and Montabone, L. (2016) Martian polar vortices: comparison of reanalyses. *Journal of Geophysical Research*, 121, 1770–1785

Young, R.M.B. (2014) The Lorenz energy cycle in simulated rotating annulus flows. *Physics of Fluids*, 26(056), 602

Zalucha, A.M., Plumb, R.A. and Wilson, R.J. (2010) An analysis of the effect of topography on the Martian Hadley cells. *Journal of the Atmospheric Sciences*, 67, 673–693

How to cite this article: Scott RK, Seviour WJM, Waugh DW. Forcing of the Martian polar annulus by Hadley cell transport and latent heating. *Q J R Meteorol Soc*. 2020;146:2174–2190. https://doi.org/10.1002/qj.3786

APPENDIX

The latitudes ϕ_w, ϕ_s and ϕ_1 in the LH88 model are uniquely determined from the latitude of maximum heating, ϕ_0, by imposing a set of matching conditions (LH88, their eqs. 8–11). These lead to a system of three equations in the unknowns ϕ_w, ϕ_s and ϕ_1, which we provide here for ease of reproducibility. In terms of a sine-latitude coordinate $y = \sin\phi$, and writing $y_0 = \sin\phi_0$, etc., the matching conditions yield the system

$$\frac{({y_s}^2 - y_1^2)^2}{1-{y_s}^2} - \frac{({y_w}^2 - y_1^2)^2}{1-{y_w}^2} - 2R[(y_s - y_0)^2 - (y_w - y_0)^2] = 0,$$

$$\left(\frac{({y_s}^2 - y_1^2)^2}{1-{y_s}^2} - 2R(y_s - y_0)^2\right)(y_s - y_1) - I[y_s] + I[y_1] + \frac{2}{3}R[(y_s - y_0)^3 - (y_1 - y_0)^3] = 0,$$

$$\left(\frac{({y_w}^2 - y_1^2)^2}{1-{y_w}^2} - 2R(y_w - y_0)^2\right)(y_w - y_1) - I[y_w] + I[y_1] + \frac{2}{3}R[(y_w - y_0)^3 - (y_1 - y_0)^3] = 0,$$

where

$$I[y] = -\frac{1}{3}y^3 - y + 2y_1^2 y + \frac{1}{2}(1 - y_1^2)^2 \log\frac{1+y}{1-y}.$$

The system can be solved by a suitable iterative scheme (e.g., Broyden, 1965). Notice that the solution y_1, y_s, y_w depends only on the latitude of maximum heating y_0 and the combination of the heating strength and the planetary Burger number $R = B\Delta$.